JOURNAL OF PROPULSION AND POWER
Vol. 17, No. 2, March–April 2001

Experimental Testing of a Hypersonic Inlet with Rectangular-to-Elliptical Shape Transition

M. K. Smart*
NASA Langley Research Center, Hampton, Virginia 23681

Wind-tunnel testing of a hypersonic inlet with rectangular-to-elliptical shape transition has been conducted at Mach 6.2. These tests were performed to validate the use of a recently developed design methodology for fixed-geometry hypersonic inlets suitable for airframe integrated scramjets. Results indicated that flow features within the inlet were similar to design and that the inlet typically captured 96% of the available airflow. Typical mass-flow-weighted total pressure recoveries of 55% were obtained for compression ratios of 14.8 throughout the test program. Assessment of the inlet starting characteristics indicated that the inlet self-started at Mach 6.2 despite the fact that it had an internal contraction ratio well above the Kantrowitz limit (Kantrowitz, A., and Donaldson, C., "Preliminary Investigation of Supersonic Diffusers," NACA WR L-713, 1945). These results demonstrate that high-performance, fixed-geometry inlets can be designed to combine a nearly rectangular capture with a smooth transition to an elliptical throat.

Nomenclature

A, C, E, G, I, K	=	pressure instrumentation streamlines
A_{FM}	=	flow meter throat area
C_D	=	discharge coefficient for the mass-flow meter
Cp_{Ni}	=	specific heat of nickel
H	=	enthalpy, zero-base reference
M	=	Mach number
m_c	=	mass capture percentage
$\dot{m}$	=	mass flow rate
P_{av}	=	average pressure on instrumentation streamlines
P_R	=	inlet compression ratio, p_e/p_1
P_T	=	inlet total pressure recovery, $p_{t,e}/p_{t,1}$
p	=	pressure
q	=	dynamic pressure
$\dot{q}$	=	heat transfer rate
R	=	gas constant for air, 287.035 J/kg K
Re	=	Reynolds number
T	=	temperature
T_R	=	inlet temperature ratio, T_e/T_1
t	=	time
u	=	x component of velocity
v	=	volume
x	=	axial length along model
y	=	height
z	=	width
γ	=	ratio of specific heats
η_{KD}	=	process efficiency, $\dfrac{1-(P_R)^{(1-\gamma)/\gamma}}{1-(T_{t,1}/T_{t,e})(P_R/P_T)^{(1-\gamma)/\gamma}}$
η_{KE}	=	kinetic energy efficiency, $\dfrac{T_{t,e}}{T_{t,1}}\left[1-\dfrac{2/(\gamma-1)}{M_1^2}\left\{(P_T)^{(1-\gamma)/\gamma}-1\right\}\right]$
ρ	=	density

Subscripts

c	=	stagnation chamber
cap	=	inlet capture
e	=	inlet exit
i	=	inside cowl
m	=	model
o	=	outside cowl
t	=	total
t_2	=	pitot
w	=	wall
1	=	inlet entrance

Received 30 September 1999; revision received 28 February 2000; accepted for publication 9 March 2000.

*NRC Research Associate; currently Aeronautical Engineer, Lockheed Martin Engineering and Sciences, NASA Langley Research Center, MS 168, Hampton VA 23681. Senior Member AIAA.

Introduction

THE design of efficient inlets for hypersonic vehicles utilizing airframe integrated scramjet modules is a subject of interest in the high-speed propulsion community. In these configurations, the vehicle bow shock performs the initial compression, and the capture shape for the inlet of each scramjet module is required to be rectangular. Other requirements are that inlets start before ramjet takeover speeds are reached (Mach 3–4), that they operate over a large Mach number range, and that they be efficient during vehicle cruise. For overall system simplicity there is also a strong desire to have an intake with fixed geometry and no requirement for boundary-layer bleed. Another desirable feature of a hypersonic inlet for some scramjet applications is a transition from a rectangular capture to an elliptical throat. The inlet may then be used in combination with an elliptical combustor, which is superior to a rectangular combustor in terms of the structural weight required to withstand a specified pressure/thermal load, and the wetted surface area needed to enclose a specified cross-sectional area. This type of configuration also reduces the undesirable effects of hypersonic corner flows.

A number of three-dimensional curved inlets leading to circular or elliptical combustors were designed and tested in the 1960s.[1–4] These fixed-geometry inlets performed well during wind-tunnel tests and self-started with internal contraction ratios considerably above the one-dimensional theoretical starting limit first introduced by Kantrowitz and Donaldson.[5] The current study involves a further investigation of the advantages of three-dimensional curved inlets, a task greatly simplified by the advent of modern computational tools. These tools have enabled a design methodology to be devised for hypersonic inlets in which all internal surfaces of the inlet perform a portion of the compression, corners are removed with a minimum of disturbance to the flow, and three-dimensional shock cancellation is utilized. All of these features contributed to the design of a high-performance inlet configuration that includes a transition from a

nearly rectangular capture to an elliptical throat. A detailed methodology for the design of fixed-geometry, rectangular-to-elliptical shape transition (REST) inlets was reported in Ref. 6. The current paper describes the experimental testing of a Mach 6.0 REST inlet in a hypersonic wind tunnel with a freestream Mach number of 6.2.

Experimental Program

Wind-Tunnel and Test Conditions

The current experiments were conducted in the NASA Langley Research Center Arc Heated Scramjet Test Facility (AHSTF).[7] In this facility, an electric arc heats a portion of the airflow to approximately 4450 K, and the remaining airflow is injected downstream of the arc heater to produce the desired test conditions. The AHSTF can provide test flows with a total enthalpy corresponding to Mach 8 flight. In the current tests, however, actual flight total enthalpy was not required, and the AHSTF was operated at low temperature to maximize Reynolds number ($12.0–15.6 \times 10^6$/m) and to meet model temperature restrictions. The Mach 6.2 nozzle used for the tests had a 27.7×27.7 cm exit and exhausted into a 1.22 m (4 ft) diam test chamber that was connected to a 30.5 m (100 ft) vacuum sphere.

AHSTF Mach 6.2 nozzle calibrations are reported in Ref. 8 for a range of wind-tunnel total conditions. These indicated that the nozzle flow contains vortex pairs at the midpoint of each wall that contaminate the core flow. The inlet was, therefore, positioned so that its projected capture tube contained as high a proportion of undisturbed core flow as possible. Figure 1 shows the inlet capture stream tube superimposed on a contour plot of the nozzle exit Mach number for a typical test condition, indicating that the inlet captured only a small portion of the flow affected by the vortex pairs. Two nominal test points were established for the experimental program. Table 1 lists the facility stagnation chamber conditions for these test points and the equivalent one-dimensional properties of the flow within the inlet capture stream tube. These values were generated by scaling the nozzle calibration data[8] at stagnation chamber conditions $p_c = 2.24$ MPa (325 psia) and $H_c = 0.614$ MJ/kg (264 Btu/lbm) to the test points utilized in the current program.

Experimental Model

A photograph of the fully assembled experimental model mounted in the AHSTF test section is shown in Fig. 2. The complete model consisted of the REST inlet, a cruciform rake, a dump-isolator tube, a mass-flow meter, and supporting structure. Three views of the fully assembled model are shown in Fig. 3, with key dimensions labeled. The complete model was approximately 175 cm (69 in.) in length and was suspended in the test section from two overhead I-beam sections. The inlet had a total length of 94.6 cm (37.2 in.), with cowl closure 50.8 cm (19.9 in.) from the most forward point, the throat a further 28.6 cm (11.3 in.) downstream of cowl closure, and a 15.2 cm (6-in.) long elliptical isolator downstream of the throat. The capture area of 113.8 cm^2 (17.6 in.^{2}) was 15.2 cm (6.0 in.) wide and 11.0 cm (4.3 in.) high at its plane of symmetry and had sharp leading edges. The inlet was manufactured from pure nickel using an electroforming technique. The first step in this process involved the machining of an aluminium mandrel to the internal shape and surface finish required for the inlet. This was followed by nickel deposition to approximately 3.5 mm thickness, final machining, and then removal of the mandrel by the use of an acid bath. This overall process provided an economical means of manufacturing the three-dimensional curved internal shape to within the desired tolerance of ±0.13 mm (±0.005 in.).

The fixed-geometry inlet was designed using the methodology outlined in Ref. 6. This method combined a quasi-streamtraced inviscid technique with a correction for three-dimensional boundary-layer growth, to design an inlet with nearly rectangular capture and

Table 1 Wind-tunnel test conditions

Property	Test point 1	Test point 2
p_c, MPa (psia)	3.01 (437)	2.67 (390)
H_c, MJ/kg (Btu/lbm)	0.702 (302)	0.556 (239)
M_1	6.18	6.18
p_1, kPa (psia)	1.393 (0.202)	1.241 (0.180)
T_1, K (°R)	81.1 (145.9)	64.0 (115.3)
$p_{t,1}$, MPa (psia)	2.672 (387.5)	2.366 (343.1)
$T_{t,1}$, K (°R)	690 (1242)	550 (991)
$Re_1 \times 10^6$, m^{-1} (ft^{-1})	12.0 (3.66)	15.6 (4.77)
q_1, kPa (psf)	37.3 (779)	33.2 (694)
$\dot{m}_1$, kg/s (lb/s)	0.757 (1.669)	0.760 (1.675)
Capture area, cm^2 (in.^{2})	113.8 (17.64)	113.8 (17.64)

Fig. 2 Photograph of the fully assembled REST inlet model in the AHSTF test section.

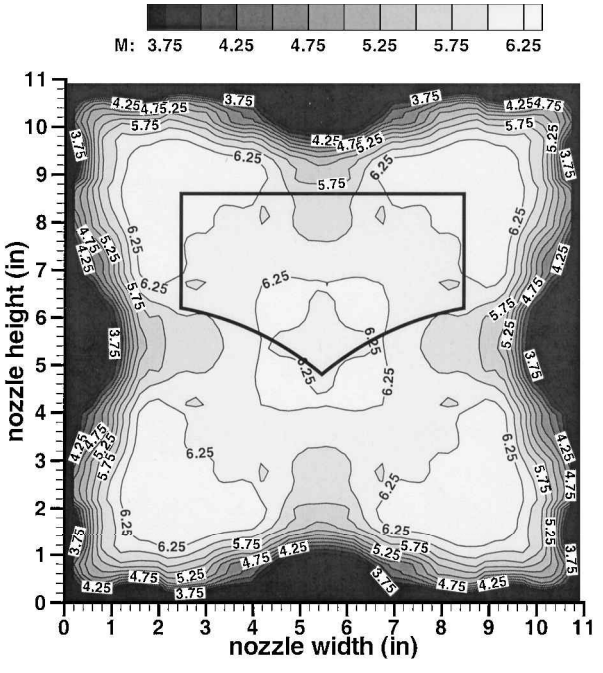

Fig. 1 Mach number contours at the Mach 6.2 nozzle exit with the REST inlet capture area shown.

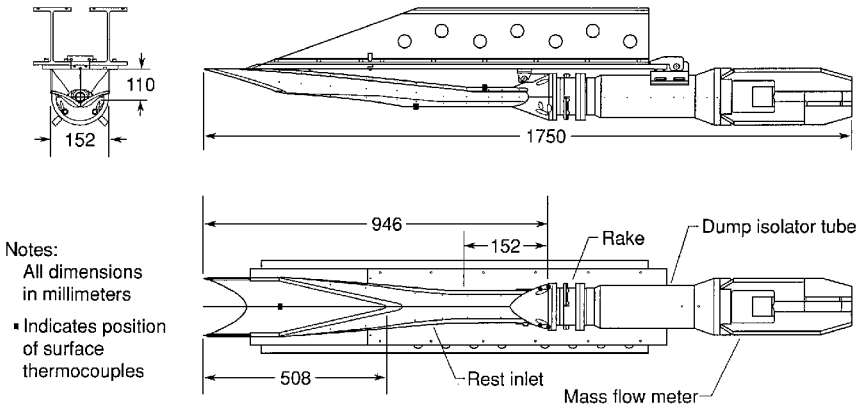

Fig. 3 Three views of the REST inlet model configuration.

smooth transition to an elliptical throat. Its highly notched cowl was designed to allow for flow spillage when operating below the design Mach number. The particular inlet shown in Figs. 2 and 3 was designed to be mounted beneath a vehicle cruising at Mach 7.1 on a constant $q = 50$ kPa (1044 psf) trajectory. In combination with a 6 deg forebody compression, the inlet was required to supply a scramjet combustor with flow at, or above, 50 kPa (0.5 atm). In this instance, flow enters the inlet at $M_1 = 6.0$, and the required inlet compression ratio is $P_R = 13.5$. Further assumptions used in the design of the model were an entrance Reynolds number of $Re_1 = 26 \times 10^6$/m, a wall-to-total temperature ratio of $T_w / T_{t,1} = 0.5$, and a transition to turbulent flow that began 1.25 cm (0.5 in.) downstream of all leading edges. The resulting inlet model had an overall contraction ratio of 4.74 and an internal contraction ratio of 2.15.

The cruciform rake mounted at the rear of the inlet contained both pitot and static pressure probes for surveying the inlet exit flow. An 8.9 cm (3.5 in.) diameter dump-isolator tube was connected to the rear of the rake. Fueled engine operation was simulated by reducing the exit area of the dump isolator via translation of a conical plug. Throughout the test program, this device was used to 1) obtain an estimate of the inlet mass capture and 2) examine the self-start capability and back-pressured performance of the inlet.

Instrumentation and Data Acquisition

Model instrumentation consisted of surface pressure taps, pitot and static pressure probes, coaxial surface thermocouples, and total temperature probes. Model pressures were measured using a Pressure Systems, Inc., Model 8400 electronically scanning pressure system. Four pressure ranges were utilized in the tests: 0–6.8 kPa (0–1 psia), 0–34.4 kPa (0–5 psia), 0–102.1 kPa (0–15 psia), and 0–680.7 kPa (0–100 psia). The error associated with the use of these transducers was ±0.5% of full scale. The type E coaxial surface thermocouples were manufactured by Medtherm Corporation and were electrically isolated from the model. The error associated with the use of these thermocouples was ±0.5% of the temperature measured above the 273 K reference. The type K thermocouples used in the total temperature probes were of beaded construction, and the error associated with the use of the total temperature probes was ±0.75% of the temperature measured above the 273 K reference. Thermocouple output was converted to temperature by a universal temperature reference system and processed by a 16-bit NEFF A/D converter. Facility data were also processed by the NEFF A/D converter. All data recorded using the Autonet Version 4.0 data acquisition software on a personal computer. Pressure data associated with the model recorded at a rate of 10 Hz, and all thermocouple and facility data recorded at a rate of 50 Hz. All error bars shown in the paper were calculated using standard uncertainty analysis techniques and the aforementioned instrumentation error ranges.

Figure 4 shows a schematic of the nominal streamlines along which surface pressure taps were distributed in the inlet. Pressure taps were concentrated on the right-hand side of the model (as the model had a vertical plane of symmetry) and were placed on the six streamlines (labeled A, C, E, G, I, and K in Fig. 4) at 15 different axial stations along the inlet. These instrumentation streamlines were approximately equally spaced around the internal surface of the inlet and gave a good indication of the overall surface pressure distribution. Thermocouples were placed at three representative positions on the inside surface of the model, that is, the front of the inlet, downstream of the inlet throat, and on the cowl just downstream of the inlet crotch (see Fig. 3). These were used to monitor the temperature of the inlet and also to obtain an estimate of the heat transfer to the model.

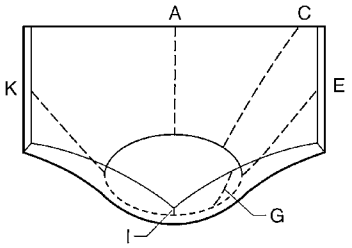

Fig. 4 Schematic of the REST inlet pressure instrumentation streamlines.

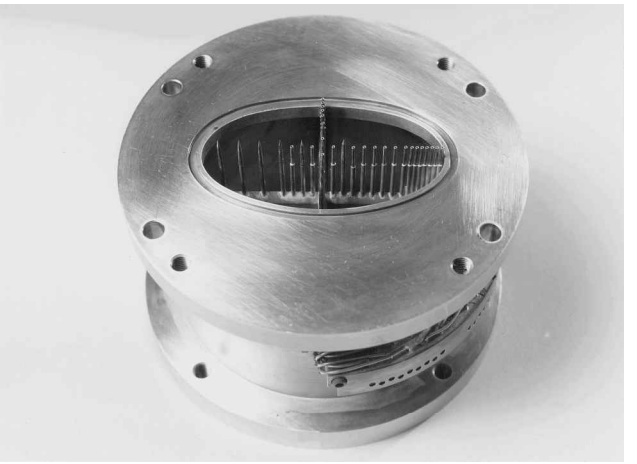

Fig. 5 Photograph of the cruciform rake containing both pitot and static probes.

A photograph of the cruciform rake is shown in Fig. 5. It contained 24 pitot probes with an outer diameter of 1.0 mm and 12 static probes with an outer diameter of 1.5 mm. The static probes were equally spaced along the horizontal and vertical branches of the rake, whereas the pitot probes were concentrated near the walls to measure the viscous losses in the inlet more accurately. The static probes were designed for internal supersonic flow measurements using the method of Pinckney.[9] A full pitot and static pressure survey of the inlet exit flow required two runs, with the cruciform rake rotated 180 deg between runs.

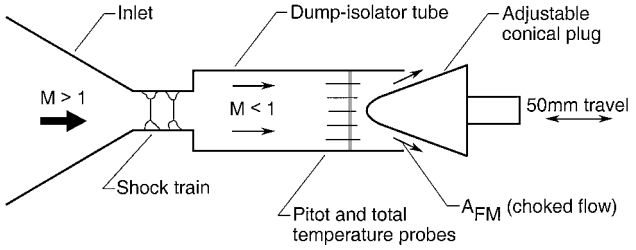

Fig. 6 Schematic of the flow meter and the back-pressured flowfield.

Figure 6 shows a schematic of the device used to measure the captured inlet mass-flow rate. These measurements were obtained by back pressuring the inlet/dump isolator with the conical plug until a shock train was stabilized near the throat of the inlet. Flow was then subsonic in the dump isolator and choked at its exit. In the current apparatus (referred to in the remainder of the paper as the flow meter), four pitot probes and two total temperature probes were situated slightly upstream of the conical plug to obtain values for the pitot pressure and total temperature of the flow exiting the flow meter. Assuming a thermally perfect gas and a sonic Mach number at the throat of the flow meter, the captured inlet mass-flow rate is then given by

$$\dot{m}_{\text{cap}} = p_t(p/p_t)\sqrt{(\gamma/RT_t)(T_t/T)}C_D A_{\text{FM}} \tag{1}$$

where p/p_t, γ, and T/T_t are all functions of T_t and are calculated using the methods described in Ref. 10. The discharge coefficient for the mass-flow meter, $C_D = 0.978$, was obtained from a previously performed calibration. The error associated with the mass-flow rate calculations was estimated at $\pm 1.7\%$.

Test Program

The test program was separated into two sections, 1) determination of the inlet starting characteristics and back-pressured performance and 2) determination of the inlet efficiency, capability, and mass capture. The starting characteristics of the REST inlet were assessed by reducing the exit area of the flow meter until the inlet unstarted, then removing the flow constriction. Restarting of the inlet after such a mechanically imposed unstart is generally considered to be definitive proof that the inlet will self-start at similar conditions. The maximum back pressure tolerated by the inlet before unstart is also an important design parameter because it provides an indication of the amount of pressure rise that the inlet will withstand during dual-mode scramjet engine operation.

To define the conditions of the air entering the combustor of a scramjet engine, both an inlet efficiency term, like total pressure recovery, as well as an inlet capability term, like compression ratio, must be supplied.[11] The mass-flow rate of the air captured by the inlet is also required. The efficiency, capability, and mass capture of the REST inlet were determined using the pitot and static pressure surveys at the inlet exit plane, the surface pressure distributions within the inlet, and the flow meter measurements. Run times of 35 s allowed the effect of different wall temperature conditions to be investigated, but the model was never allowed to reach adiabatic wall conditions due to the temperature limit of the epoxy used to seal the surface pressure taps (500 K). Test section Reynolds number and dynamic pressure were varied as indicated in Table 1.

Results and Discussion

Inlet Starting Characteristics

If the inlet did not start, then no useful data could be obtained from the tests. Hence, inlet start-ability, both with the initial tunnel startup and after mechanically induced unstarts, was critical to the test program. As discussed in Ref. 12 and other places, the key parameter for characterizing inlet starting is the Mach number at its plane of closure. Based on computational fluid dynamics analyses, the mass-flow averaged Mach number at the cowl closure plane in the current experiments was $M_{\text{cap}} = 4.68$. The Kantrowitz limit[5] indicates a maximum internal contraction of 1.53 at Mach 4.68. The REST inlet was designed with an internal contraction ratio of 2.15, so it violated the generally used rule of thumb for inlet starting by a significant margin. Despite this, the REST inlet was observed to start with the wind tunnel for all test conditions. Figure 7 shows a schlieren image of a typical test. Flow is from left to right and the external shock structure generated by the inlet can be seen at the bottom of the image. The appearance of a cowl shock emanating from the crotch of the inlet was found to be a good indicator that the inlet was started.

Figure 8 shows an instantaneous schlieren image of the external shock structure observed during a mechanically induced unstart. This flowfield exhibited high-amplitude fluctuations, with a strong shock oscillating well upstream of the inlet crotch. Figure 9 shows

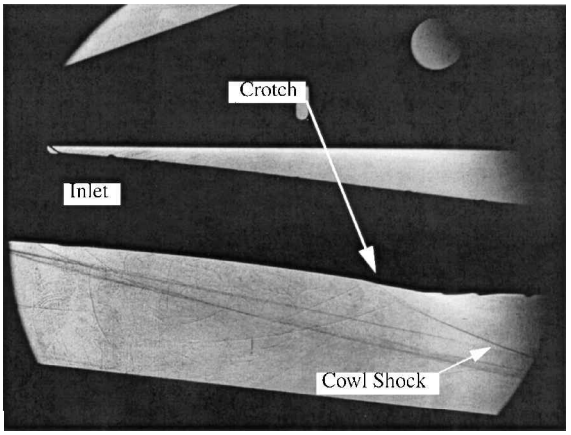

Fig. 7 Schlieren image of the started flowfield.

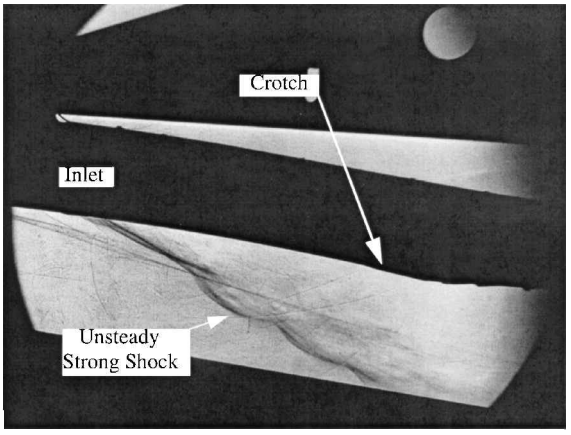

Fig. 8 Instantaneous schlieren image of the highly unsteady unstarted flowfield.

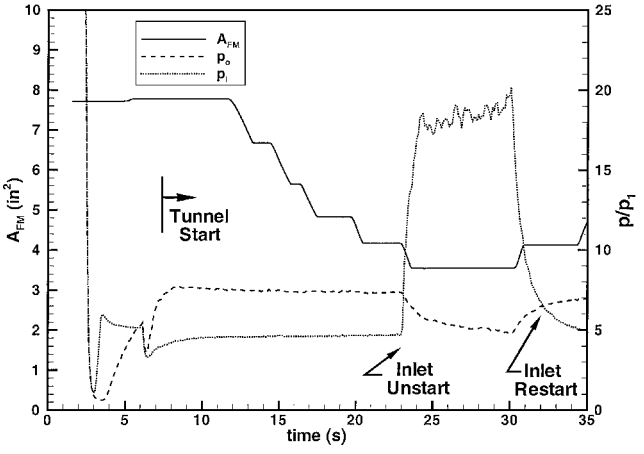

Fig. 9 Plot of the flow meter throat area and the key surface pressures vs time during a self-start test.

Table 2 Comparison of actual and design test conditions

Property	Actual	Design
M_1	6.18	6.0
$Re \times 10^6$, m^{-1} (ft^{-1})	12.0/15.6 (3.66/4.77)	26.0 (7.92)
$T_w/T_{t,1}$	0.44–0.71	0.50

a time-dependent plot of flow meter throat area A_{FM} and two key surface pressure taps during a typical unstart test. These taps were situated just downstream of the inlet crotch, one on the inner surface of the inlet and one on the outer surface. The behavior of these two pressure measurements gave a clear indication of whether the inlet was started or not. During a self-start test, A_{FM} was gradually reduced until unstart was observed. This flow process is indicated in Fig. 9 by the crossing over of the p_i and p_o pressures traces. After a period in which the inlet remained unstarted, an increase of A_{FM} allowed the inlet to restart at an area slightly larger than the area at which the unstart began. The REST inlet tested in the current experiments exhibited the ability to self-start after mechanically induced unstarts for all test conditions.

Surface and Probe Based Pressure Measurements

The REST inlet tests were initially planned to be undertaken in the NASA Langley Research Center 20 in. Mach 6 tunnel, but the tests were transferred to the AHSTF due to scheduling difficulties. For this reason, the test Mach number and Reynolds number were slightly different from design. Table 2 shows a comparison of the actual test conditions with those used to design the REST inlet. Whereas the wall thermal conditions of the tests were similar to design, both the increased Mach number and the decreased Reynolds number produced a higher inlet compression ratio than the design value of $P_R = 13.5$.

Figure 10 shows the normalized surface pressure distributions along instrumentation streamlines A, C, E, G, and I (see Fig. 4) for test point 1 with $T_w/T_{t,1} = 0.438$, together with the design values. In the portion of the inlet upstream of the crotch, the experimental data was almost identical to the design values. Downstream of the crotch, experimental data showed some differences in local pressure levels, but the overall trend of the experimental and design pressure distributions remained similar. The local discrepancies observed downstream of the crotch are believed to be due to features of the shock/boundary-layer interactions not accounted for in the design process (see Ref. 6). The results shown in Fig. 10 are typical of the surface pressure distributions observed throughout the test program. It was generally observed that the inlet surface pressure distributions were somewhat sensitive to the wall thermal condition, but exhibited minimal sensitivity to the changes in Reynolds number between the two test points.

Both the pitot and static pressure distributions at the exit of the inlet were measured using the cruciform rake. In combination with the mean total temperature of the flow at the inlet exit, these measurements were used to calculate a complete set of properties at each probe location, assuming the air behaved as a thermally perfect gas. To determine the total temperature of the inlet exit flow, an estimate of the average heat transfer rate to the model $\dot{q}_m$ was obtained using

$$\dot{q}_m = \frac{dT_m}{dt} C p_{Ni}\, \rho_{Ni}\, v_m \qquad (2)$$

As noted earlier, the inside surface temperature was measured at three representative locations on the model (see Fig. 3). As the model was a thin-walled structure (wall thickness ≈3.5 mm), the temperature gradient of the entire structure dT_m/dt was assumed to be equal to the average of the three representative surface temperature gradients. Employing the specific heat of nickel Cp_{Ni}, the density of nickel ρ_{Ni}, and the volume of the model v_m, use of Eq. (2) resulted in typical heat transfer rates to the model of between 0.6% and 1.5% of the captured total enthalpy flux. Subtracting the heat transfer rate from the captured total enthalpy flux gave the total enthalpy flux of the flow exiting the inlet. The methods described in Ref. 10 were used to calculate the total temperature corresponding to the exit flow enthalpy flux.

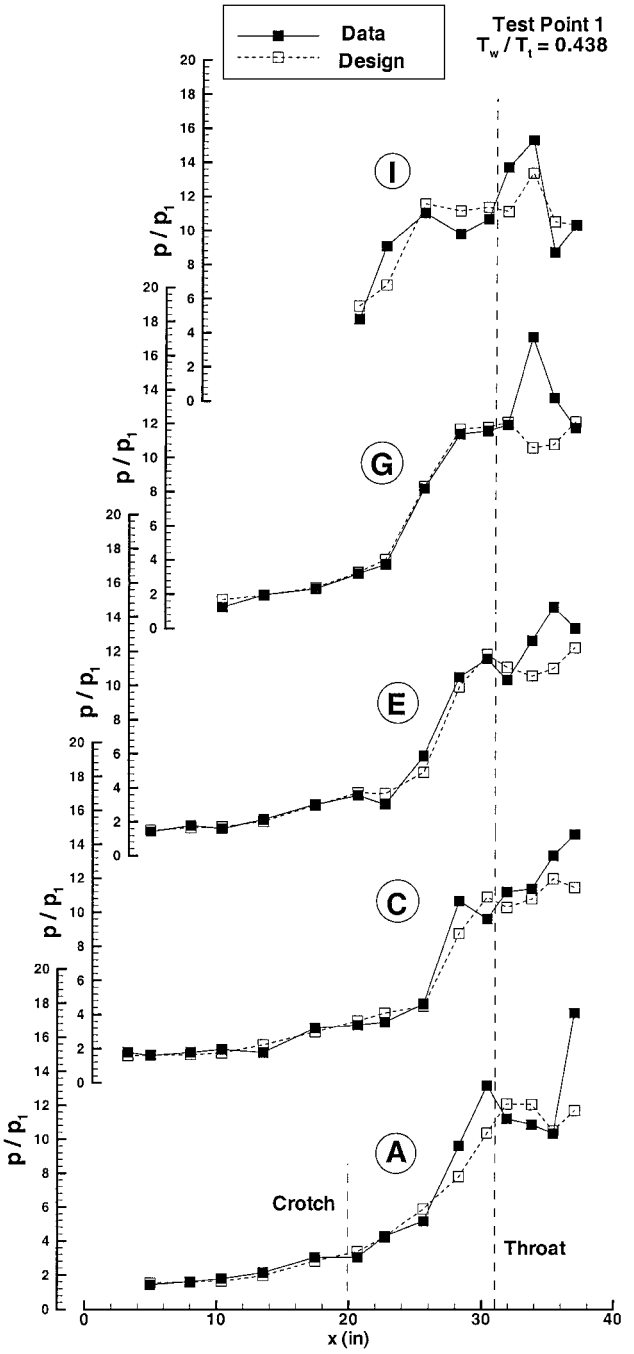

Fig. 10 Surface pressure comparison between design and experiment along instrumentation streamlines.

Figures 11a and 11b show the normalized pitot and static pressure distributions obtained along the horizontal and vertical branches of the rake for test point 2 with $T_w/T_{t,1} = 0.631$. Figure 11a indicates that both the p_e and $p_{t2,e}$ distributions are nearly symmetric about the centerline of the inlet. Interestingly, p_e was observed to be approximately constant across the horizontal branch, whereas, $p_{t2,e}$ showed plateaus near both walls, smooth peaks approximately midway between the center and walls, and a central dip. The dip in $p_{t2,e}$ at the center of the inlet was an unexpected feature of the flow, especially given the relatively constant p_e. Probe interference and other possible problems associated with the central pitot probes were investigated as causes of this phenomenon, without result. It is

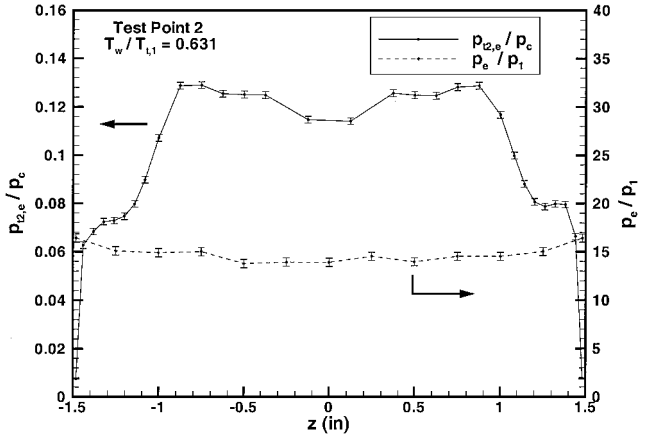

a) Horizontal branch

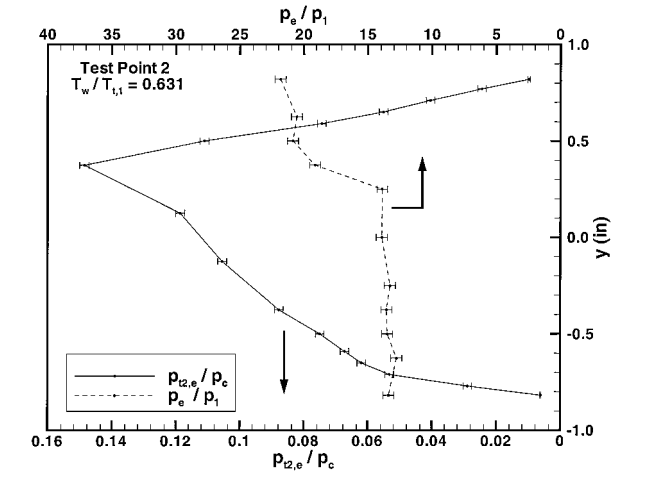

b) Vertical branch

Fig. 11 Pitot and static pressure probe measurements at the inlet exit.

possible that the central dip in $p_{t2,e}$ is a consequence of the nonuniformities present in the inlet capture flow (Fig. 1) because the inlet was designed with the assumption of uniform freestream flow. Figure 11b shows that p_e remained constant on the lower two-thirds of the vertical branch, then jumped to a level approximately 50% higher on the upper one-third. The corresponding $p_{t2,e}$ distribution peaked toward the top of the inlet and exhibited a sharp dip in the viscous-dominated region near the top wall. On the bottom portion of the vertical branch, $p_{t2,e}$ dropped from its peak at a more gradual rate due to increased shock losses near the cowl. These distributions are typical of those observed at the exit of the inlet throughout the test program.

Figures 12a and 12b show the Mach number and total pressure distributions calculated from the rake measurements. On the horizontal branch (Fig. 12a) both M_e and $p_{t,e}$ show a similar shape to $p_{t2,e}$, with the Mach number peaking at $M_e = 3.9$ approximately halfway between the center and the wall and dipping to $M_e = 3.5$ at the center. In general, the presence of the central dip in pitot pressure had a significant effect on all of the calculated inlet flow properties. The vertical branch distributions of M_e and $p_{t,e}$ (Fig. 12b) were also similar to $p_{t2,e}$ with the Mach number peaking at $M_e = 3.8$ toward the top of the inlet exit. Note that the distribution of $\rho_e u_e$ (not shown) was also observed to show a similar trend to the distribution of $p_{t2,e}$.

Inlet Efficiency, Capability, and Mass Capture

Equivalent one-dimensional mass-flow-weighted properties have been calculated at the inlet exit using the probe measurements. These were generated by dividing the inlet exit area into four sections, then constructing a series of elliptical-annular strips centered on each of the pitot probe positions on the horizontal and vertical branches of the rake. The properties at the pitot probe positions were then assumed to correspond to the average values over the strip. When integrated over the entire exit area of the inlet, this averaging technique was expected to supply a best possible one-dimensional estimate of the inlet performance, given the available data. Table 3 includes a complete list of the exit flow properties corresponding to the data shown in Figs. 11 and 12.

Table 3 Equivalent one-dimensional properties at the inlet exit for test point 2[a]

Property	Test point 2
p_t, MPa (psia)	1.269 (184.0)
T_t, K (°R)	543.6 (978.4)
H_t, MJ/kg (Btu/lb)	0.548 (235.8)
M	3.264
p, kPa (psia)	18.76 (2.721)
T, K (°R)	181.3 (326.3)
ρ, kg/m^3 (lb/ft^3)	0.377 (2.35 × 10^{-2})
u, m/s (ft/s)	854.4 (2803)
$\dot{m}$ kg/s (lb/s)	0.732 (1.615)
Area cm^2 (in.^{2})	24.37 (3.778)

[a] $T_w / T_{t,1} = 0.631$.

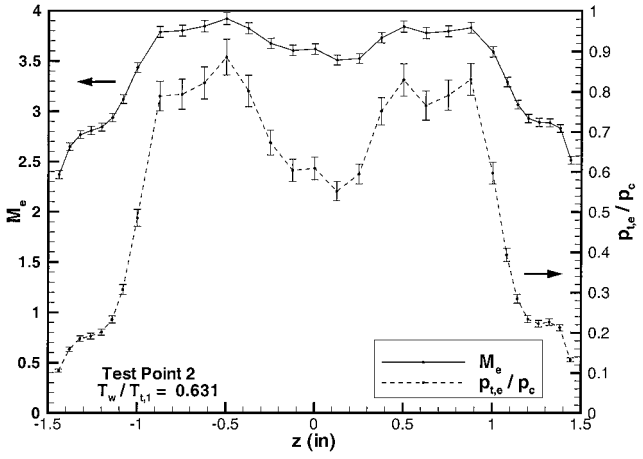

a) Horizontal branch

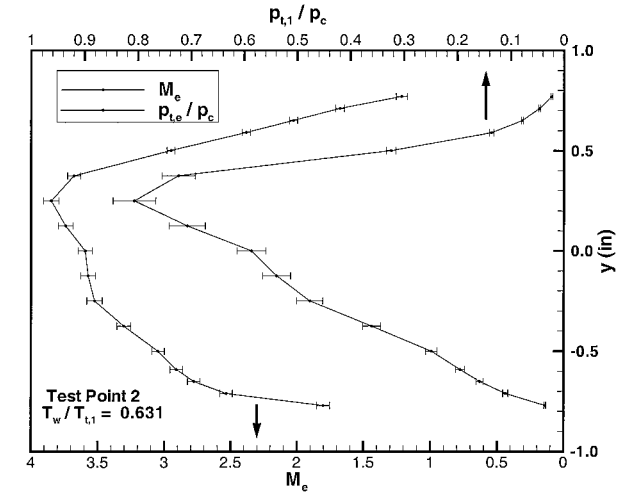

b) Vertical branch

Fig. 12 Calculated Mach number and total pressure ratio at the inlet exit.

Numerous experiments were conducted at both test points with different wall temperature conditions. Figure 13 shows plots of mass-flow-weighted equivalent one-dimensional efficiency parameters, namely, the total pressure recovery P_T, the kinetic energy efficiency η_{KE}, and the process efficiency η_{KD}, vs wall-to-total temperature ratio $T_w / T_{t,1}$. Note from Fig. 13 that the efficiency curves for both test points are almost identical where they overlap. This indicated that the 30% difference in Reynolds number between test points 1 and 2 had a minimal effect on inlet efficiency. Also note

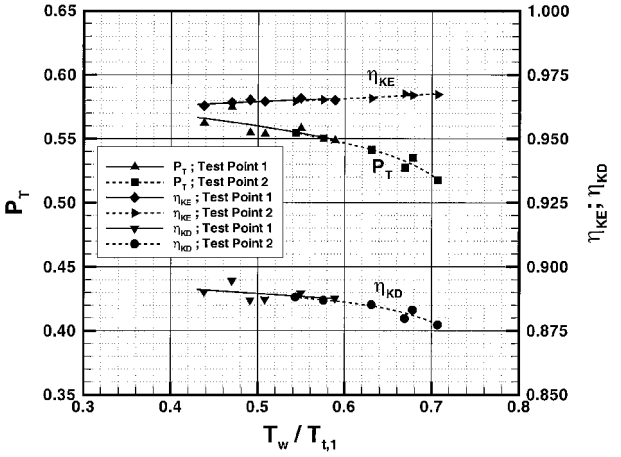

Fig. 13 Plots of inlet efficiency parameters vs wall-to-total temperature ratio.

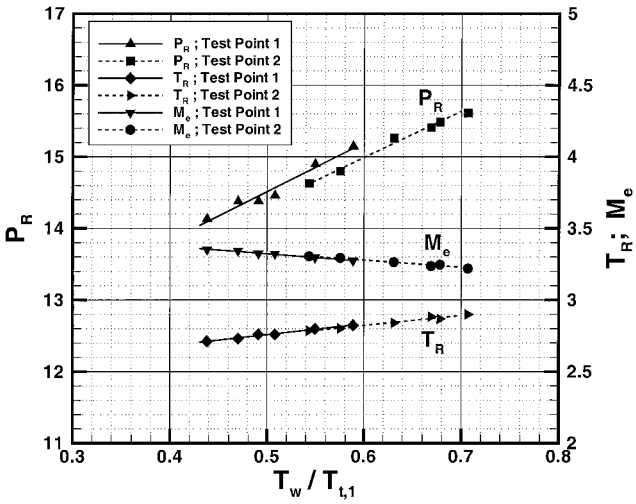

Fig. 14 Plots of inlet capability parameters vs wall-to-total temperature ratio.

from Fig. 13 that $T_w/T_{t,1}$ had a significant effect on P_T. For example, increasing $T_w/T_{t,1}$ from 0.44 to 0.71 reduced P_T from 0.565 to 0.517. This decrease in P_T was due to the increased boundary-layer thickness for the higher $T_w/T_{t,1}$. Process efficiency showed a less pronounced decrease with increasing $T_w/T_{t,1}$, with values in the range $\eta_{KD} = 0.895$–0.877 for the tests. In contrast to P_T and η_{KD}, kinetic energy efficiency showed a slight increase with increasing $T_w/T_{t,1}$, with values in the range $\eta_{KE} = 0.963$–0.968 for the tests.

The wall-to-total temperature ratio effect was also manifested in the inlet capability, as indicated by parameters like compression ratio P_R, temperature ratio T_R, and exit Mach number M_e, which are plotted vs $T_w/T_{t,1}$ in Fig. 14. The increased boundary-layer thickness for the higher $T_w/T_{t,1}$ values raised the pressure and temperature ratio by increasing the aerodynamic contraction experienced by the inviscid core flow. The same phenomenon also reduced the Mach number at the inlet exit. Increase of $T_w/T_{t,1}$ from 0.44 to 0.71 produced a 10.7% increase in P_R to a maximum for the current tests of $P_R = 15.55$. Both T_R and M_e showed a less pronounced dependence on $T_w/T_{t,1}$ with typical values of $T_R = 2.81$ and $M_e = 3.29$.

Table 4 lists the ranges of the mass-flow-weighted equivalent one-dimensional values for P_R, T_R, M_e, P_T, η_{KE}, and η_{KD} measured for the REST inlet at the two test points. The values listed in Table 4 correspond to mass capture percentages of $m_c = 96.0$ and 96.6% for test points 1 and 2, respectively. Both of these values are within the error range of the corresponding mass-flow meter measurements, which were $m_c = 96.2 \pm 1.7\%$ and $96.5 \pm 1.7\%$ for test points 1 and 2, respectively.

Table 4 Equivalent one-dimensional performance parameter ranges for test points 1 and 2

Property	Test point 1, $T_w/T_{t,1} = 0.44$–0.59	Test point 2, $T_w/T_{t,1} = 0.54$–0.71
P_R	14.10–15.18	14.65–15.55
T_R	2.72–2.84	2.79–2.90
M_e	3.35–3.28	3.32–3.22
P_T	0.565–0.544	0.555–0.512
η_{KE}	0.963–0.966	0.965–0.968
η_{KD}	0.895–0.887	0.888–0.877
m_c	$96.2 \pm 1.7\%$	$96.5 \pm 1.7\%$
$\dot{q}_m/H_{t,1}$	1.20–0.61%	1.48–1.13%

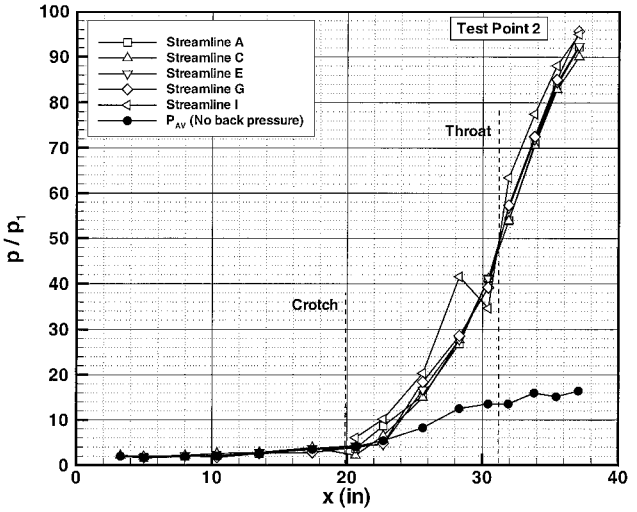

Fig. 15 Surface pressure distributions at the maximum back-pressure condition.

Inlet Back Pressure Performance

Figure 15 shows a typical pressure distribution in the inlet for test point 2 at maximum back pressure, that is, just before a mechanically induced unstart. This data supplies an indication of the maximum pressure the REST inlet could sustain in a combustor during dual-mode scramjet operation. A plot of the average pressure along the inlet without back pressure has been added to Fig. 15 for reference. Note that when fully back pressured, the axial pressure distributions along all streamlines become similar. This is an indication that flow downstream of the inlet crotch is fully separated, with a shock train situated inside the enclosed portion of the inlet. Based on the data shown in Fig. 15, the ratio of maximum back pressure to the pressure generated with no back pressure is 5.7 for this REST inlet at Mach 6.2 (note also that the maximum back pressure is approximately 90 times the freestream pressure). Measured maximum back-pressure ratios varied between 5.3 and 5.7 throughout the test program.

Conclusions

Results of Mach 6.2 wind-tunnel testing of a fixed-geometry hypersonic inlet were reported. This three-dimensional, quasi-streamtraced inlet had an overall contraction ratio of 4.74, an internal contraction ratio of 2.15, and a Mach 6.0 design point. It also included a transition from a nearly rectangular capture to an elliptical throat. The tests were conducted to validate a previously developed design methodology for fixed-geometry inlet configurations that include significant cross-sectional shape changes. The inlet was tested at a Reynolds numbers of $Re = 12.0$ and 15.6×10^6/m (3.66 and 4.77×10^6/ft) and at wall-to-total temperature ratios ranging between 0.44 and 0.71.

The inlet was observed to start with the wind tunnel at all times during the test program. It also exhibited self-starting capability after mechanically induced inlet unstarts. These results indicated that the Kantrowitz[5] starting limit does not necessarily apply to all inlet

configurations. Surface pressure distributions within the inlet were found to be similar to design. However, the overall compression ratio generated by the inlet was higher than design because the inlet was tested above the design Mach number and below the design Reynolds number. Equivalent one-dimensional performance parameters were obtained using both pitot and static pressure probes at the inlet exit. On a mass-flow-weigthed basis, capability parameters such as compression ratio and exit Mach number ranged between 14.1 and 15.6 and 3.35 and 3.22, respectively. Efficiency parameters such as total pressure recovery and kinetic energy efficiency ranged between 0.565 and 0.512 and 0.963 and 0.968, respectively. In general, increased values of wall-to-total temperature ratio led to increased inlet capability, but at a reduced total pressure recovery. Inlet mass capture was deduced from measurements to be approximately 96% of the available airflow. Heat transfer to the model ranged between 0.6% and 1.5% of the captured total enthalpy flux. Finally, back-pressurization data indicated that the maximum back-pressure ratio relative to unhindered operation varied between 5.3 and 5.7. This test program demonstrated that the inlet shape transition required to utilize elliptically shaped combustors in airframe integrated scramjets can be accomplished without sacrificing inlet performance.

Acknowledgments

This work was supported by the Hypersonic Airbreathing Propulsion Branch and the Hyper-X Program Office at NASA Langley Research Center. The author would like to thank E. Ruf and A. Auslender for many useful discussions of the work and R. Irby, J. Connover, and J. Simmons for their efforts during the test program.

References

[1]Hartill, W. B., "Analytical and Experimental Investigation of a Scramjet Inlet of Quadriform Shape," U.S. Air Force Rept. AFAPL-TR-65-74, Marquardt Corp., Aug. 1965.

[2]Billig, F. S., "Supersonic Combustion Ramjet Missile," *Journal of Propulsion and Power*, Vol. 11, No. 6, 1995, pp. 1139–1146.

[3]Kutshenreuter, P. H., "Hypersonic Inlet Tests in Helium and Air," General Electric Co. Advanced Engine and Technology Departments, Cincinnati, OH, June 1965.

[4]Molder, S., and Romeskie, J. M., "Modular Hypersonic Inlets with Conical Flow," CP-30, AGARD 1968.

[5]Kantrowitz, A., and Donaldson, C., "Preliminary Investigation of Supersonic Diffusers," NACA WR L-713, 1945.

[6]Smart, M. K., "Design of Three-Dimensional Hypersonic Inlets with Rectangular-to-Elliptical Shape Transition," *Journal of Propulsion and Power*, Vol. 15, No. 3, 1999, pp. 408–416.

[7]Guy, R. W., Rogers, R. C., Puster, R. L., Rock, K. E., and Diskin, G. S., "The NASA Langley Scramjet Test Complex," AIAA Paper 96-3243, July 1996.

[8]Thomas, S. R., Voland, R. T., and Guy, R. W., "Test Flow Calibration Study of the Langley Arc- Heated Scramjet Test Facility," AIAA Paper 87-2165, June 1987.

[9]Pinckney, S. Z., "Improved Static Probe Design," *AIAA Journal*, Vol. 12, No. 4, 1974, p. 562.

[10]Witte, D. W., and Tatum, K. E., "Computer Code for Determination of Thermally Perfect Gas Properties," NASA TP-3447, Sept. 1994.

[11]Molder, S., McGregor, R. J., and Paisley, T. W., "A Comparison of Three Hypersonic Inlets," Sec. 6, "Investigations in the Fluid Mechanics of Scramjet Inlets," U.S. Air Force Rept. WL-TR-93-2091, Ryerson Polytechnic Inst., Toronto, 1993.

[12]Van Wie, D. M., Kwok, F. T., and Walsh, R. F., "Starting Characteristics of Supersonic Inlets," AIAA Paper 96-2914, July 1996.